INTERNATIONAL JOURNAL FOR NUMERICAL METHODS IN FLUIDS
Int. J. Numer. Meth. Fluids 2008; **57**:237–263
Published online 16 October 2007 in Wiley InterScience (www.interscience.wiley.com). DOI: 10.1002/fld.1622

Numerical modeling of cohesive sediments dynamics in estuaries: Part I—Description of the model and simulations in the Po River Estuary

C. Leupi[1,*,†], M. S. Altinakar[2] and M. Deville[1]

[1]*ISE-STI-LIN, Ecole Polytechnique Fédérale, Lausanne 1015, Switzerland*
[2]*NCCHE, The University of Mississippi, Carrier Hall Room 102 University, MS 38677, U.S.A.*

SUMMARY

The present work contributes to the numerical modeling of complex turbulent multiphasic fluid flows occurring in estuarine channels. This research finds its motivation in the increasing need for efficient management of estuaries by taking into account the complex turbulent stratified flows encountered in estuaries and costal zones. A time-dependent, 3D finite element model of suspended sediment transport taking into account the effects of cohesiveness between sediments is presented. The model estuary is the forced time-dependent winds, time elevation at open boundaries and river discharge. To cope with the stiffness problems a decoupling method is employed to solve the shallow-water equations of mass conservation, momentum and suspended sediment transport with the conventional hydrostatic pressure. The decoupling method partitions a time step into three subcycles according to the physical phenomena. In the first sub-cycle the *pure hydrodynamics* including the k–ε turbulence model is solved, followed by the advection–diffusion equations for pollutants (salinity, temperature, suspended sediment concentration, (SSC)), and finally the bed evolution is solved. The model uses a mass-preserving method based on the so-called Raviart–Thomas finite element on the unstructured mesh in the horizontal plane, while the multi-layers system is adopted in vertical with the conventional conforming finite element method, with the advantage that the lowermost and uppermost layers of variable height allow a faithful representation of the time-varying bed and free surface, respectively. The model has been applied to investigate the SSC and seabed evolution in Po River Estuary (PRE) in Italy. The computed results mimic the field data well.

Received 30 September 2005; Revised 15 August 2007; Accepted 16 August 2007

KEY WORDS: cohesive sediments; finite element model; unstructured grid; turbulence model; multiplayers; salinity; temperature; bed evolution; estuary

*Correspondence to: C. Leupi, ISE-STI-LIN, Ecole Polytechnique Fédérale, Lausanne 1015, Switzerland.
†E-mail: cleupi@yahoo.fr, cleupi@bluewin.ch

Contract/grant sponsor: Swiss National Science Foundation; contract/grant number: 21-65095.01

1. INTRODUCTION

Estuaries are the meeting point between the freshwater charged with sediment from river and the saline sea cold water. Many famous ports of the world are situated in such a zone.

Every year governments spend considerable amounts of money in estuarial development, maintenance and management projects without necessarily being sure what their likely outcome and/or effectiveness will be.

The present research finds its motivation in the increasing need for efficient management of estuaries by taking into account the various conflicting environmental and socio-economical aspects.

Improvements of ports and navigation channels will result in a change in original regimes of such an estuary such as shoaling patterns, circulation patterns, salinity intrusions etc., and planning of such work requires therefore a knowledge of estuarine dynamics, sedimentation processes, sources of sediments, and location and amount of shoaling.

Laboratory scale models and field measurements are difficult to realize cost considerable amounts of money and they cannot provide satisfactory answers to all questions. Thus, the adaptive management approaches launched from numerical modeling investigations might be most appropriate for the better understanding and to obtain cost-effective results.

Many engineering and environmental flow problems involve the study of water motion in rivers, lakes and seas. They are characterized by the presence of a *free surface* and, in some cases, by a vertical scale much smaller than the horizontal one. The shallow-water equations (SWEs) with the conventional hydrostatic pressure have been successfully applied to many engineering problems and their use has become common practice in environmental impact studies in estuarial and coastal regions.

The sediment transport in estuaries involves the numerical solution of basic conservation equations for mass, momentum and turbulent energy. The Coriolis force, tidal forcing, wind action, resistance to flow at the bed, buoyancy effects due to temperature, salinity and sediment concentration, bed-level changes due to deposition and erosion should all be modeled for a realistic representation of the real-world phenomena.

In this respect, numerous research works have been carried out to establish well-validated physical and mathematical descriptions of the behavior and fate of concentrated near-bed cohesive sediment suspensions and their interaction with the water column and the bed as well as the turbulence characteristics of sediment laden flow.

Lie-Yauw and Mellor [1, 2] have applied a 3D finite difference model for simulation of the Hudson–Raritan Estuary with a second-order turbulence-closure sub-model. Lu and Wai [3] developed an efficient operator splitting scheme for 3D hybrid hydrodynamic model using the so-called *sigma transformation* in the vertical direction. Chau and Jiang [4, 5] have developed a finite difference model based on Princeton Ocean Model (POM) with an orthogonal curvilinear coordinate in the horizontal direction and sigma coordinate in the vertical direction for simulating hydrodynamics and pollutants transport in the Pearl River Estuary.

van Rijn [6, 7] has developed a depth-integrated 2D model and a 3D model for non-cohesive sediment transport. Only 3D model was used for simulating seabed evolution. Roberts [8] used a 2D depth-averaged model to investigate the fluid mud. Ziegler and Nisbet [9] used a 2D model to study the transport of cohesive and non-cohesive sediments in Pawtuxet River in Rhode Island without simulating the seabed evolution. Guan *et al.* [10] used a 2D width-integrated model to compute sediment transport in Jiaojiang River Estuary in China. Lin and Falconner [11] used a 3D layer-integrated model to predict suspended sediment fluxes in the Humber Estuary, U.K.

DOI: 10.1002/fld

Chen *et al.* [12] have successfully applied a 3D finite difference model with hydrostatic pressure distribution for cohesive sediment transport by tidal currents and the resulting bed-level changes to the Pearl River Estuary.

In the recent years, several European research projects were launched on estuarine modeling within the framework of MArine Science and Technology (MAST). One of the outcomes of this project was a *COupled Hydrodynamical Ecological model for Regional Shelf seas* called *COHERENS* (1999) [13], which is composed of: a physical component with modules for currents, temperature and salinity; a microplankton module for simulating biological–ecological processes; a sediment module describing the deposition and resuspension of organic and inorganic material; a Eulerian and a Lagrangian particle tracer module for simulating the transport of contaminants (e.g. radioactive and non-radioactive waste material). The model does not, however, simulate the changes in bed morphology.

Various researchers have numerically investigated the interaction between the turbulence and the sediment particles: Reynolds stress model by Teisson *et al.* [14], algebraic mixing-length model by Le Hir [15] and k–ε two-equation model by Uittenbogaard and Winterwerp [16]. Olsen and Skoglund [17] calculated sediment concentration profiles in a sand trap using k–ε turbulent model.

In many models, the settling velocity denoted by w_{ss} is taken as constant, whereas in reality it strongly depends on flocculation influenced by the turbulence intensity, salinity and temperature. Huang [18] proposed an expression of cohesive sediment settling velocity in which flocculation with effects of water temperature, settling distance sediment size and sediment concentration have been considered. Dyer [19] presented a conceptual model of the effect of shear and concentration on median floc settling velocity. The heuristic formulation of van Leussen and Corneliss [20], which relates flocculation and break-up to the dissipation rate of turbulent kinetic energy, was implemented with great success in the numerical estuary model by Malcherek *et al.* [21]. Tang [22] derived a function of critical shear stress for mixtures of cohesive and non-cohesive sediments. Mehta and Srinivas [23] studied the entrainment between the water column and the fluid mud.

Guan *et al.* [10] used a 2D width-integrated model for simulating Jiaojiang River Estuary in China. Lin and Falconner [11] used a 3D layer-integrated model to predict suspended sediment fluxes in the Humber Estuary, U.K. Chen *et al.* [12] have successfully applied a 3D finite difference model with hydrostatic pressure distribution for simulating the Pearl River Estuary. Casulli [24] developed a stable and accurate semi-implicit finite difference scheme for the solution of the 2D SWEs with a Eulerian–Lagrangian method (ELM) for the approximation of the convective terms. This scheme was successfully extended to the three dimensions by Casulli and Chen [25].

Most of the existing models use varying degrees of parameterization in order to simplify the equations to be solved and it should be noticed that most of these existing models use an approach based on a topographically conform, sigma-transformed grid which, regardless of the depth, forces the same number of divisions in the water column. However, these uniform grid structures cannot fit to complicated geometry and this may induce large errors if applied to complex boundary configurations.

In the present paper, on the basis of the above-mentioned literature the Reynolds-averaged Navier–Stokes (RANS) equations are solved in the framework of the SWE, and a suitable two-equation k–ε closure model is adopted to account for buoyancy effects encountered in multiphasic fluid flows. Hydrodynamics is solved using implicit time marching scheme, while discretization is conducted using Euler or Runge–Kutta scheme to obtain a set of algebraic equations. The horizontal grid is built on the xy-plane unstructured triangular grid. The vertical grid is located at predefined heights and the number of elements in the water column depends on water depth (the number of

DOI: 10.1002/fld

active (wetted) layer is defined at each time step, and the vertical grid is regenerated at each time step). The lowermost and uppermost elements of variable height allow a faithful representation of the bed and the time-varying free surface, respectively. Advection–diffusion equations are solved for the transport of pollutants such as salinity, concentration and temperature to account to the variable density fluid present in the estuaries. A new set of equations for the solid transport modeling of the deposition and erosion processes (see Chen *et al.* [12]) will be incorporated in the model to investigate the suspended sediment concentration (SSC) and seabed evolution of Po River Estuary (PRE) in Italy.

An outline of this paper is as follows: In Section 2, we review the governing equations and the associated boundary conditions. In Section 3, we introduce the discretization of the physical domain, the finite element approximation and the space–time discretization. In Section 4, we propose some results by simulating the real estuarine channel with the aim of outlining the performance of the model.

2. HYDRODYNAMIC PROBLEMS

A brief description of the hydrostatic version with the turbulent model is provided in Leupi and Altinakar [26]. Let us consider an incompressible fluid body in a 3D time-varying domain $\widehat{\Omega}$ in Figure 1. Let Ω be the projection of $\widehat{\Omega}$ on the xy horizontal plane, bounded by the free-surface Γ_s given by $z=\eta(x,y,t)$, the bottom topography Γ_b given by $z=-h(x,y)$, the open boundary denoted by Γ_o. Here $h(x,y)$ is the distance between the bottom and the reference plane xy, and $\eta(x,y,t)$ the elevation of the free surface with respect to the reference plane xy.

For $t>0$ and $(x,y,z)\in\widehat{\Omega}(t)$, and from the RANS description of the turbulent motion using the Boussinesq approximation [27] under hydrostatic pressure we can write

$$\frac{1}{\rho}\frac{\partial p}{\partial z}=-g \Rightarrow p=p_a+\rho g(\eta-z) \tag{1}$$

where p_a is the atmospheric pressure.

The system of the SWEs for long waves (vertical scale is negligible compared with the horizontal one) for a variable density fluid reads

$$\begin{gathered}
\nabla_{xy}\cdot\mathbf{U}+\frac{\partial w}{\partial z}=0\\
\frac{\mathrm{D}\mathbf{U}}{\mathrm{D}t}-\frac{\partial}{\partial z}\left(\nu_T\frac{\partial\mathbf{U}}{\partial z}\right)+g\nabla\eta+g\nabla\left(\int_z^\eta\frac{\Delta\rho}{\rho_0}\,\mathrm{d}z\right)=\mathbf{F}_{xy}\\
\frac{\partial\eta}{\partial t}+\nabla\cdot\int_{-h}^{\eta}\mathbf{U}\,\mathrm{d}z=\tilde{F}_b\\
\frac{\mathrm{D}\zeta}{\mathrm{D}t}-\nabla\cdot\left[c_\zeta\frac{k^2}{\varepsilon}\nabla\zeta\right]=F_\zeta\quad\text{for }\forall\zeta=(k,\varepsilon)\\
\frac{\mathrm{D}\Phi}{\mathrm{D}t}-\nabla_{xy}\cdot(\nu_T\nabla\Phi)-\frac{\partial}{\partial z}\left(\nu_T\frac{\partial\Phi}{\partial z}\right)=F_\Phi,\quad\Phi=(T,S,C)\\
\rho=\rho(T,S,C)
\end{gathered} \tag{2}$$

where the unknowns are $\boldsymbol{\upsilon}$, w, η, k, ε, T and S.

DOI: 10.1002/fld

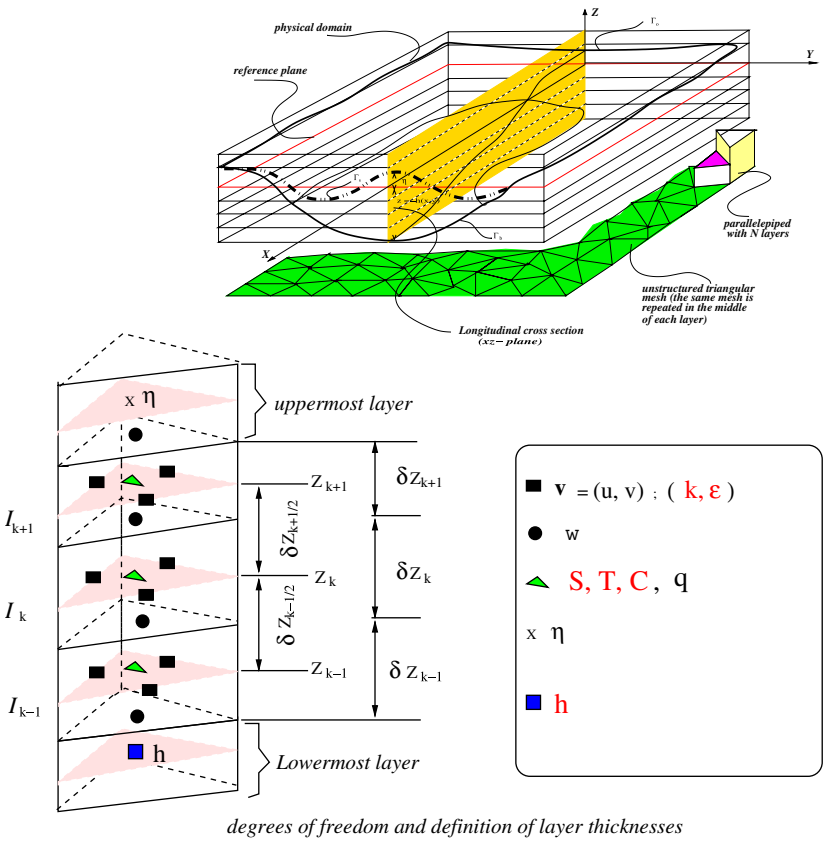

Figure 1. Physical domain representation with numerical variables location.

$\mathbf{U}=(u,v)^{\mathrm{T}}$ is the horizontal velocity vector, $\mathbf{F}_{xy}=(\mathrm{f}v,-\mathrm{f}u)^{\mathrm{T}}$ is the vector of body forces with f the Coriolis parameter, g the gravitational acceleration, and v_T the eddy viscosity, (see Rodi [28]). $\nabla\cdot$ is the 3D divergence operator, $\mathrm{D}/\mathrm{D}t$ represents the material time derivative, and $\nabla_{xy}\cdot$ is the surface divergence operator. ρ, ρ_0 are, respectively, the fluid density and the basic water density. $\boldsymbol{\Phi}(S,T,C)$ stands for the pollutants: salinitiy (S), temperature (T) and SSC (C) (for which S_0, T_0 and C^0 stand for the initial salinity, temperature and concentration).

The motion of the free surface is described by an alternative form of the equation, third equation of system (2), which is obtained by integrating the first equation [i.e. (local) mass balance] along the vertical coordinate by applying the Leibniz rule with the suitable kinematic boundaries conditions at the free surface and bottom.

In the present work the state-of-the-art k–ε turbulence model will be introduced to be able to account for both the homogeneous and stratified flows. The turbulence equations read (see also Leupi [29], Mohammadi and Pironneau [30]) as follows:

$$\frac{\mathrm{D}k}{\mathrm{D}t}-\nabla\cdot\left[c_\mu\frac{k^2}{\varepsilon}\nabla k\right]=c_\mu\frac{k^2}{\varepsilon}P_d-\varepsilon-\lambda_T N^2 \tag{3}$$

DOI: 10.1002/fld

$$\frac{\mathrm{D}\varepsilon}{\mathrm{D}t}-\nabla\cdot\left[c_\varepsilon\frac{k^2}{\varepsilon}\nabla\varepsilon\right]=c_1 k P_d-\frac{\varepsilon}{k}[c_3\lambda_T N^2+c_2\varepsilon] \tag{4}$$

The squared shear frequency or production term P_d reads as

$$P_d=\tfrac{1}{2}(\|\nabla\mathbf{V}+\nabla\mathbf{V}^{\mathrm{T}}\|)^2 \tag{5}$$

where $\|.\|$ is the 2-norm of the matrix. The model constants are given as: $c_1=0.126$, $c_2=1.92$, $c_\mu=0.09$, $c_\varepsilon=0.07$. In the above equations, N is the Brunt–Väisälä frequency, with the related following squared buoyancy N^2 (see COHERENS [13]) expression,

$$N^2=-\frac{\nu_T}{\sigma_t}\frac{g}{\rho_0}\frac{\partial\rho}{\partial z} \tag{6}$$

Here $\sigma_t=1$ is a constant, and the following expressions of eddy coefficients ν_T, λ_T should include the stability parameters to account for the turbulence damping in the stratified fluid flows (see Luyten *et al.* [31], COHERENS [13]):

$$\nu_T=S_u\frac{k^2}{\varepsilon}+\nu,\quad \lambda_T=S_b\frac{k^2}{\varepsilon}+\lambda_b \tag{7}$$

$$S_u=\frac{0.108+0.0229\alpha_N}{1+0.471\alpha_N+0.0275\alpha_{N^2}},\quad S_b=\frac{0.177}{1+0.403\alpha_N} \tag{8}$$

where $\lambda_b=10^{-6}$, and the stability coefficients α_N and c_3 can be expressed as

$$\alpha_N=\frac{k^2}{\varepsilon^2}N^2 \tag{9}$$

$$c_3=\begin{cases}-0.4 & \text{for } N^2<0\\ 1 & \text{otherwise}\end{cases} \tag{10}$$

In system (2), the state equation for the variable density can be written as follows:

$$\begin{aligned}\rho_l&=\alpha(S-S_0)+\beta(T-T_0)\\ \rho&=\rho_l+(\frac{\rho_s-\rho_l}{\rho_s})C\end{aligned} \tag{11}$$

where α and β are the known coefficients, ρ_s, ρ are, respectively, the sediment and water density.

2.1. Boundary and initial conditions

At the bottom, the no-slip condition is applied together with a zero normal velocity component to Γ_b. This second condition can be represented by

$$w_b=u_b\frac{\partial h}{\partial x}+v_b\frac{\partial h}{\partial y}=0\quad \text{on } \Gamma_b \tag{12}$$

The equilibrium assumption is adopted at the bed (i.e. the local balance between production of turbulent kinetic energy and the rate of dissipation). The wall functions are applied to relate

DOI: 10.1002/fld

the velocity to the bed shear velocity u_* in the rough turbulent boundary layer, i.e. at the distance, δ_n, normal to the nearest wall, such that $30\nu/u_* < \delta_n < 100\nu/u_*$ (see Leupi *et al.* [32], Roland [27]).

At free surface Γ_s, the kinematic condition reads as

$$w_s = \frac{\partial \eta}{\partial t} + u_s \frac{\partial \eta}{\partial x} + v_s \frac{\partial \eta}{\partial y} \quad \text{on } \Gamma_s \tag{13}$$

Dirichlet boundary conditions are applied for the dynamic boundary condition (for shear stress due to the wind) and for turbulent quantities (see Stansby and Zhou [33]).

At the open outlet boundary denoted by Γ_o, this is a fictitious boundary used for computational purposes and on it the effect of the outside is taken into account. Typically, we impose the elevation as a function of time, i.e. $H(x, y, t) = H_0(x, y, t)$ where for all $(x, y) \in \gamma_{fo}$, H_0 is a prescribed function of t. The Neumann boundary conditions are applied for the velocity ($\partial \mathbf{V}/\partial n = 0$), and other variables (i.e. a zero normal gradient through these surfaces). At the vertical wall Γ_c, the slip boundary conditions are used by setting all normal components to the vertical wall equal to zero ($\mathbf{V}_n = 0$), and Neumann boundary conditions are applied for turbulent quantities.

3. MORPHODYNAMIC PROBLEMS

The seabed mud-fluid layer is modeled using semi-empirical functions to predict deposition and erosion rates [12]. In the sequel, h is the height in between the bottom and the xy reference plane.

3.1. Advection–diffusion equation for suspended sediment concentration

A cohesive sediment model is constructed using combined semi-empirical functions to predict the seabed sediment deposition and erosion rates. As a reminder, the advection–diffusion equation for the suspended sediment transport reads

$$\frac{\mathrm{D}C}{\mathrm{D}t} - \nabla_{xy} \cdot (\nu_{T,s} \nabla C) - \frac{\partial}{\partial z}\left[(\nu_{T,s}) \frac{\partial C}{\partial z} \right] = F_s + \omega_{\mathrm{ss}} \frac{\partial C}{\partial z} \tag{14}$$

where C (kg/m^3) is the sediment concentration, $\nu_{T,s}$ (m^2/s) is the vertical mixing coefficients, ω_{ss} (m/s) is the settling velocity of sediment particles, F_s (m^3/s) is the net flux of suspended sediment

$$\nu_{T,s} = \zeta_s \phi \nu_T \tag{15}$$

On the basis of the experimental data of Coleman [34], the factor ζ_s was found to be in the range of 1–3, and we chose $\zeta_s = 1$. The damping factor for local concentration ϕ reads [35] as follows:

$$\phi = 1 + \left[\frac{C}{C^0} \right]^{0.8} - 2 \left[\frac{C}{C^0} \right]^{0.4} \tag{16}$$

For concentration smaller than 1%, one can take a value of $\phi = 1$.

DOI: 10.1002/fld

3.2. Bottom conditions

The bed morphology evolution Δz must be defined to close the so-called *integrated continuity equation* (third equation of system (2)), and its right-hand side in the bottom layer can be written as

$$\int_{\Omega} \tilde{\mathbf{F}}_b \, \mathrm{d}\Omega = \int_{\Omega} \int_0^{T_s} \frac{\partial h}{\partial t} \psi \, \mathrm{d}t \, \mathrm{d}\Omega = \Delta z |\Omega| \tag{17}$$

where T_s represents the solid flow time scale (which is in general much higher than the hydrodynamic time scale). The following lines deal with the parameterization of the bed morphology for the sediment transport. This bed evolution accounts for three processes including the bed fresh deposit layer, Δz, the partially consolidated and the fully consolidated bed.

To solve Equation (14), the boundary conditions and the physical parameters associated with the sediment and flow properties must be known. The boundary conditions are given as the sediment concentration at the river upstream intake and the sediment exchanges at the water surface, open boundaries and seabed. The vertical sediment exchange, noted as F_s, is defined by the net flux of the sediment which reads as

$$F_s = D - E, \quad D = \omega_{\mathrm{ss}} C, \quad E = -\nu_{v,s} \frac{\partial C}{\partial z} \tag{18}$$

This net flux of the sediment in the vertical direction expressed as the difference in the downward sediment flux, D, and the upward sediment flux, E. The net vertical sediment transport is assumed to be zero at the water surface boundary, resulting in $F_s = 0$. At the seabed the net flux sediment is considered as the difference in the deposition to the bed, noted as D_b, and the sediment entrainment from the bed, noted as E_b. For uniform sediments, the deposition rate is proportional to the concentration and can be expressed as the production of the settling velocity and sediment settling probability that accounts for the turbulent parameter and physical features of the bed sediments

$$D_b = \alpha_s \omega_{\mathrm{ss}} C \tag{19}$$

where α_s is the probability of the sediment settling with the range [0,1].

The settling (fall/rise) velocity of the flocculated granule, ω_{ss}, expressed from Stokes function van Rijn [36] reads as

$$\omega_{\mathrm{ss}} = D_{50}^2 g \frac{(\rho_m - \rho_0)}{18 \nu C_h \rho_0} \tag{20}$$

where D_{50} is the mean sediment particle size and C_h is the Chezy's coefficient. The suspended cohesive sediment in seawater usually have flocculated structures. It should be pointed out that the settling velocity of the flocculated granule is much larger than that of the particles in dispersive state. The smaller the sediment particle diameter size is, the stronger the flocculation ability may be. To express such effects, Migniot [37] used a flocculation factor L such that

$$L = \frac{\omega_{L_{50}}}{\omega_{D_{50}}} \tag{21}$$

where $\omega_{L_{50}}$ is the flocculation limited settling velocity and the $\omega_{D_{50}}$ is the sand particle velocity without flocculation.

DOI: 10.1002/fld

A function ω_L has been derived by Huang [18] for sediment velocity combined with water temperature, settling distance, particle size and sediment concentration:

$$\omega_L = \omega_{ss}\left[1-\left(\frac{L-1}{L}\right)e^{-KC_0Z_b}\right], \quad L=7.25D_{50}^{-2} \tag{22}$$

where $K=0.012$ is constant, C_0 is the initial sediment volumetric concentration and Z_b is the settling distance.

The entrainment rate from seabed is assumed to be a function of flow parameters and physical features of bed sediments:

$$E_b=\begin{cases}0 & \text{for } \tau_b\leqslant\tau_{b,cr}\\ -\nu_{v,s}\left(\dfrac{\partial C}{\partial z}\right)_{z=a}=\alpha_s\omega_{ss}C_a & \text{for } \tau_b>\tau_{b,cr}\end{cases} \tag{23}$$

where C_a the near-bed equilibrium reference concentration at level $a=0.01h$ above the bottom (value with water depth averaged) reflects the capacity to carry sediment by current. Under currents based on field measurement and flume tests and based on energy considerations, Dou *et al.* [38], (also Chen *et al.* [12]) derived the function of reference concentration for silty particles at level $a=0.01h$ above seabed such that

$$C_a=\alpha\frac{\rho\rho_s}{\rho_s-\rho}\left(\frac{n_s^2u_a^3}{h^{4/3}\omega_{ss}}\right) \tag{24}$$

in which u_a is the current velocity at level a; $\alpha=0.0067$ is a constant coefficient; n_s ($m^{-1/3}/s$) is the Strickler coefficient defined as $n_s=R_h/C_h$, and R_h (m) is the hydraulic radius Graf and Altinakar [39].

$\tau_{b,cr}$ is the critical erosion bed shear stress. τ_b is the bed shear stress that is expressed as follows:

$$\tau_b=\nu_T\sqrt{\left[\left(\frac{\partial u}{\partial z}\right)^2+\left(\frac{\partial v}{\partial z}\right)^2\right]} \tag{25}$$

On the basis of the information obtained from field measurements and experiments, Tang [22] derived a function for incipient bed sediment motion velocity for the sediment particle size ranging from 1 to 1.25×10^5 μm, such that

$$u_{b,cr}=\vartheta\bar{u}_{b,cr}=\left[3.2\left(\frac{\gamma_s-\gamma}{\gamma}\right)gD_{50}+\frac{\xi}{\rho^*D_{50}}\right]^{1/2} \tag{26}$$

in which $u_{b,cr}$ is the bottom sediment incipient velocity; $\bar{u}_{b,cr}$ is the vertical averaged critical velocity and

$$\vartheta=\frac{\left(\dfrac{m+1}{m}\right)}{\left(\dfrac{h}{D_{50}}\right)^{1/m}}, \quad m=0.47\left(\frac{H}{D_{50}}\right)^{0.06} \tag{27}$$

DOI: 10.1002/fld

where $\gamma_s = \rho_s g$, and $\gamma = \rho g$ are the voluminal weight of, respectively, sediment and water [40], ρ_s is the sediment density. $\xi = 2.9 \times 10^{-5}\,\mathrm{kg/m}$ and $\rho^* = 102\,\mathrm{kgs^2/m^4}$ are the given coefficients related to viscous effects.

The critical shear stress can be expressed as follows:

$$\tau_{b,\mathrm{cr}} = \frac{1}{77.5}\left[3.2(\gamma_s - \gamma)D_{50} + \frac{\xi}{D_{50}}\right] \tag{28}$$

The soft-mud layer thickness, Δz, can be calculated using the following expression [12, 38]:

$$\Delta z = \frac{\alpha_s \omega_{\mathrm{ss}}}{\gamma_0}(C - \beta C_a)\Delta\tau \tag{29}$$

in which γ_0 is the dry sediment density, β is a coefficient and $\Delta\tau$ is the solid flow time step.

In Equation (29), the coefficient, β, is defined as

$$\beta = \begin{cases} 1, & C > C_a \\ 1, & C \geqslant C_a \quad \text{and} \quad \tau_b > \tau_{b,\mathrm{cr}} \\ \dfrac{C}{C_a}, & C \leqslant C_a \quad \text{and} \quad \tau_b \leqslant \tau_{b,\mathrm{cr}} \end{cases} \tag{30}$$

4. SPACE–TIME DISCRETIZATION

The physical 3D domain (Figure 1) is embedded in a parallelepiped composed of $\mathcal{N}$ layers and the full description can be found in Leupi and Altinakar [26]. The horizontal components of the velocity vector are defined at the middle of edges of the triangular mesh elements, while the vertical component is associated with the lower horizontal faces of the element.

The horizontal velocity is approximated combining the lowest order Raviart–Thomas element ($\mathbb{RT}_0$) in xy-plane with the $\mathbb{P}_1$ elements along the vertical direction. For every integer $r \geqslant 0$ we denote by $\mathbb{P}_r(T)$ the space of polynomials of degree $\leqslant r$ on each triangle $T \in \mathscr{T}_h$ (see Figure 1) and consider the Raviart–Thomas vector finite element space of lowest order $\mathbb{RT}_0$ (see Leupi *et al.* [32], Raviart and Thomas [41]), with the following functional spaces $H_{0,c}(\mathrm{div};\Omega) = \{\boldsymbol{\tau} : \boldsymbol{\tau} \in (L^2(\Omega))^2, \mathrm{div}\,\boldsymbol{\tau} \in L^2(\Omega), \boldsymbol{\tau}\cdot\mathbf{n} = 0 \text{ on } \Gamma_c\}$, Γ_c denotes the vertical solid wall. The Sobolev space $H^1(\Omega)\{\psi \in L^2(\Omega) : \partial_{x_i}\psi \in L^2(\Omega), i = 1, \ldots, d\}$ and the finite element spaces are as follows:

$$\begin{aligned}
\mathbb{Q}_h &= \{\mathbf{q} \in H_{0,c}\ (\mathrm{div};\Omega)\,|\,\mathbf{q}|_T \in \mathbb{RT}_0(T),\ \forall T \in \mathscr{T}_h\} \\
U_h &= \{\psi \in L^2(\Omega)\,|\,\psi|_T \in \mathbb{P}_0(T),\ \forall T \in \mathscr{T}_h\} \\
W_{I^1_{1/2}} &= \{\varphi \in C^0([-h,\eta])\,|\,\varphi|_{I_{k+1/2}} \in \mathbb{P}_1(I_{k+1/2}),\ \forall I_{k+1/2} \in \mathscr{I}_{1/2}\} \\
W_{I^1_1} &= \{\zeta \in C^0([-h,\eta])\,|\,\zeta|_{I_k} \in \mathbb{P}_1(I_k),\ \text{with } \zeta|_{-h} = 0 \text{ and } \zeta|_{\eta} = 0,\ \forall I_k \in \mathscr{I}_1\} \\
W_{I^0_1} &= \{\chi \in L^2(\Omega)\,|\,\chi|_k \in \mathbb{P}_0(p),\ \forall I_k \in \mathscr{I}_1\}
\end{aligned} \tag{31}$$

DOI: 10.1002/fld

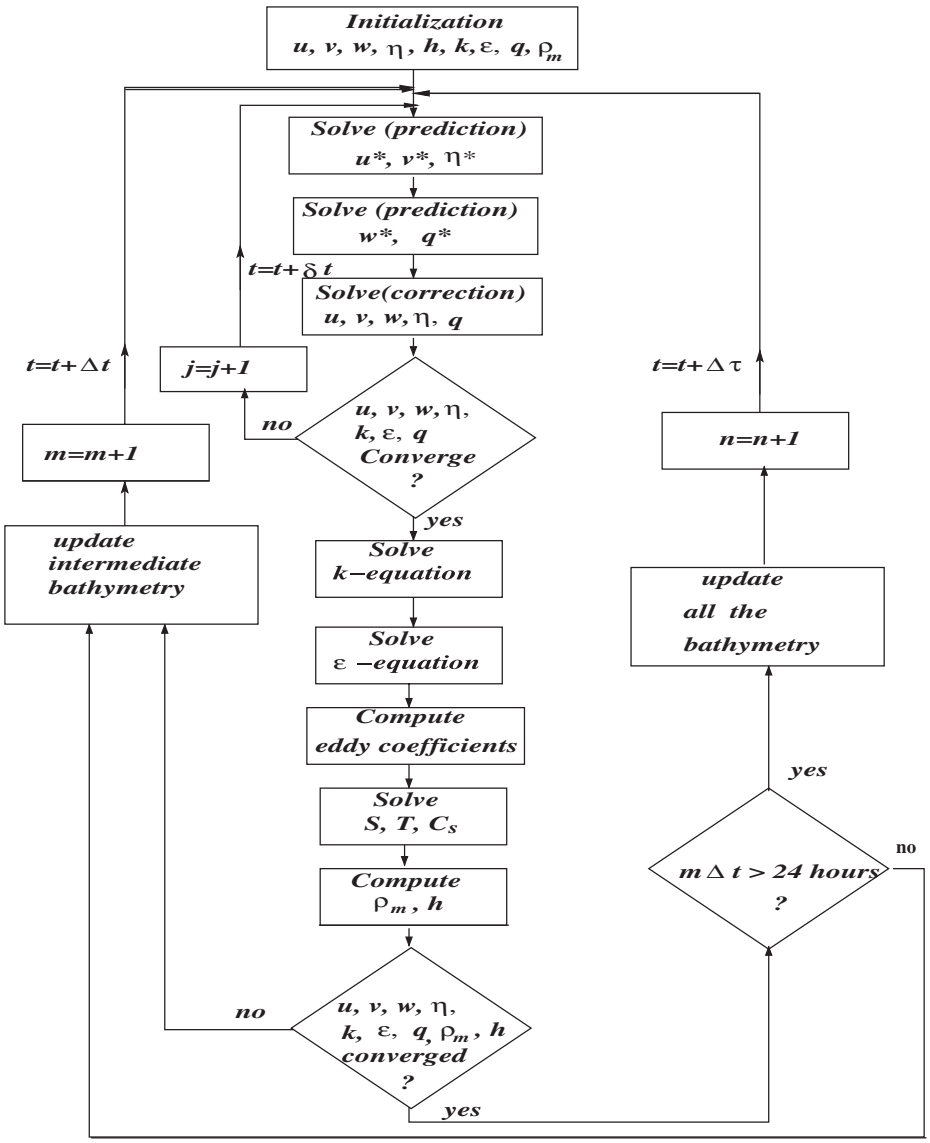

Figure 2. The flowchart of overall iterative procedure of the computations.

The approximation solutions for the variables read as

$$\mathbf{U}_h^{n+1}(\mathbf{x}, z) = \sum_{k=k_0}^{\mathscr{K}} \sum_{l=1}^{N_{\mathrm{ed}}} J^{n+1} \boldsymbol{\tau}_l(\mathbf{x}) \varphi_k(z) \quad \forall \boldsymbol{\tau} \in \mathbb{Q}_h \quad \forall \varphi \in W_{\mathscr{J}^1_{1/2}}$$

$$\eta_h^{n+1}(\mathbf{x}) = \sum_{j=1}^{N_{\mathrm{el}}} \eta_j^{n+1} \psi_j(\mathbf{x}) \quad \forall \psi \in U_h$$

DOI: 10.1002/fld

$$w_h^{n+1}(\mathbf{x},z)=\sum_{s=1}^{N_{\mathrm{el}}}\sum_{k=k_0}^{\mathscr{K}-1} w_{s,h}^{n+1}\psi_s(\mathbf{x})\zeta_{k+1/2}(z)\quad \forall\psi\in U_h\ \ \forall\zeta\in W_{\mathscr{I}_1^1}$$

$$k_h^{n+1}(\mathbf{x},z)=\sum_{s=1}^{N_{\mathrm{el}}}\sum_{k=k_0}^{\mathscr{K}-1} k_{s,h}^{n+1}\psi_s(\mathbf{x})\chi_k(z)\quad \forall\psi\in U_h\ \ \forall\chi\in W_{\mathscr{I}_1^0} \tag{32}$$

$$\varepsilon_h^{n+1}(\mathbf{x},z)=\sum_{s=1}^{N_{\mathrm{el}}}\sum_{k=k_0}^{\mathscr{K}-1} \varepsilon_{s,h}^{n+1}\psi_s(\mathbf{x})\chi_k(z)\quad \forall\psi\in U_h\ \ \forall\chi\in W_{\mathscr{I}_1^0}$$

with $_{Jl,k}=\int_{\mathrm{el}}\mathbf{V}_k\cdot\mathbf{n}_l\,\mathrm{d}\sigma, l=1,\ldots,N_{\mathrm{ed}}$.

N_{ed} and N_e denote, respectively, the number of (oriented) edges e_l and triangles T_j in the mesh, by k_0 and $\mathscr{K}$, respectively, the indice of lowermost and uppermost layers, Np, is the total number of active prisms. The Lagrange–Galerkin (or characteristics Galerkin) approach is used (see [26]) to discrezite the convection terms, while the Euler scheme or more accurate Runge–Kutta is used to obtain the algebraic system. At each time step it is only required to solve a set of the positive definite symmetric matrices for the fluxes using the conjugate gradient solver. To avoid spurious numerical oscillations, the source term, P_d, in the k equation has been discretized explicitly, the sink term has been discretized using the quasi-implicit forms and consequently the non-linear terms have been linearized (see [28, 30]). The characteristics method used here can guarantee the monotonicity of the solution (of k and ε). The model adopts the fractional time-step scheme from Mohammadi and Pironneau [30] and Leupi *et al.* [32], to solve turbulence equations. In this algorithm, the ordinary system of turbulence equations is split by first solving the convection step (containing only the terms of order zero) and the diffusion step (containing the other remaining terms) finally. Consequently, the positivity of k and ε is preserved as well as the stability of the scheme (see [32]).

5. APPLICATION TO PRE IN ITALY

In order to treat a real case and therefore demonstrate the feasibility of the method, the model is applied to investigate the dynamics in PRE in Italy.

5.1. Characteristics of PRE

PRE is located in the east of the Adriatic Sea along the direction north west–north east (NW–NE) as shown in Figure 3.

Po River (Padus River in ancient times) flows 652 km from west to east across northern Italy, from Mount Monviso (in the Cottian Alps) to the Adriatic sea near Venice. It has a drainage area of 75 000 km^2. The axis of PRE is east longitude 12.05° and north latitude 44°96667. The 75 000 km^2 river catchment of the Po is bounded at the North by the Alps with peaks over 4500 m, and at the south-west by the Apennines mountain chain with peaks generally less than 2000 m (more than a third of the drainage area (30 800 km^2) can be considered mountainous) [42]. It is the longest Italian river and goes through many important Italian towns, including Turin and (indirectly) Milan. In Milan it enters the town as a net of channels called navigli, creating a very characteristic area. Near the end of its course, it creates a wide delta (with hundreds of small channels and five main ones called Po di Maestra, Po della Pila, Po delle Tolle, Po di Gnocca and

DOI: 10.1002/fld

Figure 3. Map of the PRE and overview of the area of study.

Po di Goro). The vast valley around Po is called Pianura Padana and is so efficiently connected by the river that the whole valley became the main industrial area of the country. The tidal regime is that of a irregular diurnal micro-tidal type with the mean diurnal range of 0.80 m for the spring tide and 0.30 m for the neap tide. The M_2 main tidal component is taken into account in this study. High water levels in the North Adriatic sea caused by storms coming from the south-east, the Sirocco wind, associates to depressional fields, which move toward the East and the mean wind speed is 30–50 km/h. These events can determine oscillations with periods of 22 h and maximum amplitudes often exceeding 1 m. The data recorded by the tide gauge (of *Porto Corsini*) showed that during 1999, the maximum value of the sea level rise recorded was 1.67 m, caused by both the astronomical and the meteorological effects (see [43]). The prevailing wind and waves, which determine the main components of the solid coastal transport in the area are those from the north-east (locally called *Bora*) and the south-east (*Sirroco*). The typical characteristics for waves can be summarized as follows: (i) waves range: main orientation of the waves is 30–45° and 120–145°; (ii) maximum energetic wave $H_s = 4$ m, with a wave period of 8–9 s; (iii) mean $H_s = 1.5$–2 m, with a wave period of 5–6 s.

The PRE has two flood periods, June (freshet caused by snow melting) and November (corresponding to precipitation maxima), and two low water periods, January and August [44, 45]. The average discharge of the PRE is 1.5×10^3 m^3/s, measured at Pontelagoscuro (near Ferrara) 90 km from the coast and just before the apex of delta. Downstream of Pontelagoscuro, Po forms a delta consisting of five major distributaries (see Figure 3): the Maestra, Pilla, Tolle, Gnocca and the Goro drain, respectively, 2, 65, 12, 13, 8% of the discharge. Salinity values for the station upstream reach a maximum value of 8–20 g/l correlated with the tide cycles, while simultaneously, salt percentage measured downstream shows high salt content, up to 25–35 g/l (see [46]). The PRE

DOI: 10.1002/fld

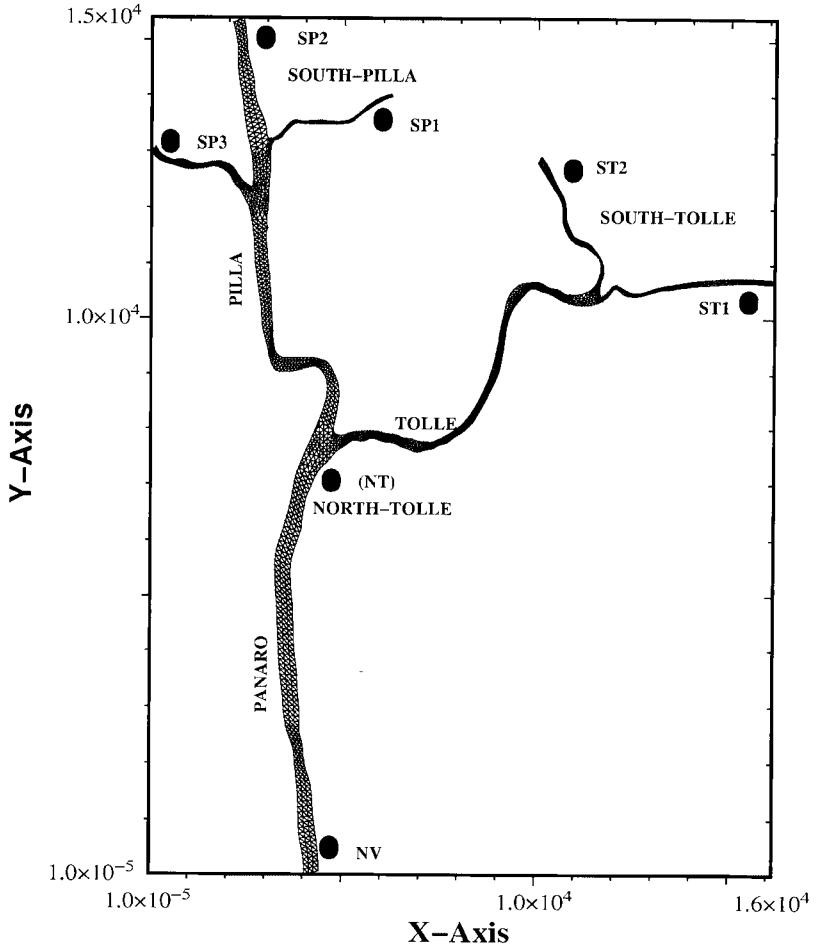

Figure 4. Two-dimensional horizontal mesh of the domain of study and tidal gauges location in Po River Estuary.

is characterized by its high level of engineering; Comprehensive and contemporary evaluations of physical, chemical and toxicological endpoints have been performed on sediments of the PRE. The particle-size composition along the PRE showed a relatively uniform distribution of fine sand, a progressive downstream decrease of coarse sands and a corresponding increase of fine materials [47]. The major sediments class is silty sand (with clay) in which the average sediments size is less than 63 μm. Hundred detailed measurements of sediment dynamics at each distributary channel have been taken. There is hardly any top set aggradation, most of sediment load is funneled to the offshore, about 16×10^6 tonnes/year, causing a high rate of fore-set propagation into the shallow northern part of Adriatic sea, while bed-load contributes only 2.5–5% of the total sediment output and high SSC. The monthly suspended sediment load was measured for the main distributary channels during six years field study [42], and may reach 300–400 mg/l in the main river stream

DOI: 10.1002/fld

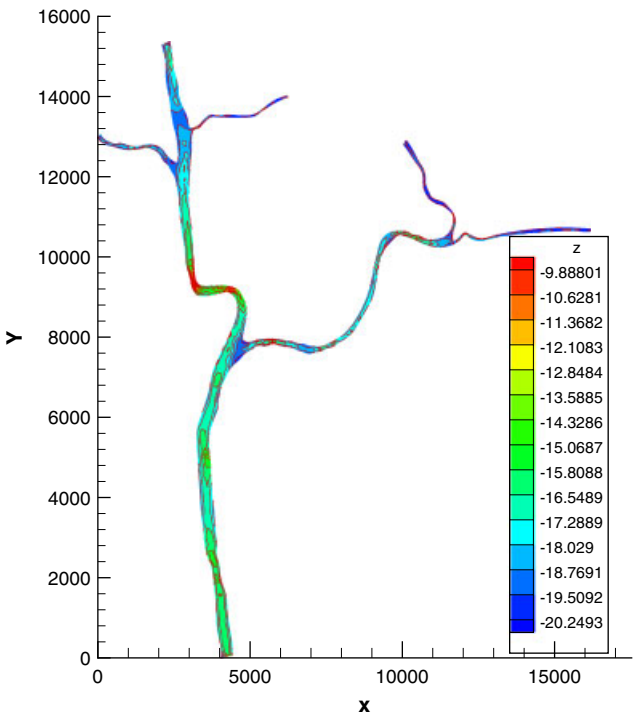

Figure 5. The bathymetry in (m) of the domain of study of Po River Estuary.

(Panaro-Pilla) and in Tolle branch, while it is around 150–300 mg/l in secondary distributaries at South-Pilla and South-Tolle (see Figure 4).

5.2. *Numerical approach*

For simulating the tidal currents and sediment transport in PRE, a large area was selected as the modeled domain called *PRE-SD* as shown in Figure 3, and the 2D horizontal plane mesh in Figure 4. The north upstream boundary has been set far upstream the five open boundaries as shown in Figure 4. The available field data for the model calibration were mostly provided by the *MOX* (*Modeling and Scientific Computing*), Department of Mathematics, Politecnico of Milano and the Istituto di ricerca Sulle Acque, CNR, Milan, Italy.

In this model, the horizontal unstructured mesh of simulated area has been divided into 3185 triangles in each horizontal layer, and 2172 nodes with the mean space step size ranging from $d^{\mathrm{T}} = 6.2$ to 46.08 m (where d^{T} denotes the diameter size of the circumscribed triangle). The vertical layer is divided into 30 layers. In account of the boundary layer effects the bottom is divided into several thin layers of thickness $\delta z_b = 0.5$ m.

The PRE bathymetry is shown in Figure 5. The simulation period is from 14:00 of 1st of May to 14:00 of 2nd May 1999 for hydrodynamic calibration. The forcing is neap tide in wet season. There are seven tide gauges and seven tide stations and water open boundaries were controlled by tidal levels and sediments concentrations located at NV, NT, ST1, ST2, SP1, SP2, SP3 (see Figure 4).

DOI: 10.1002/fld

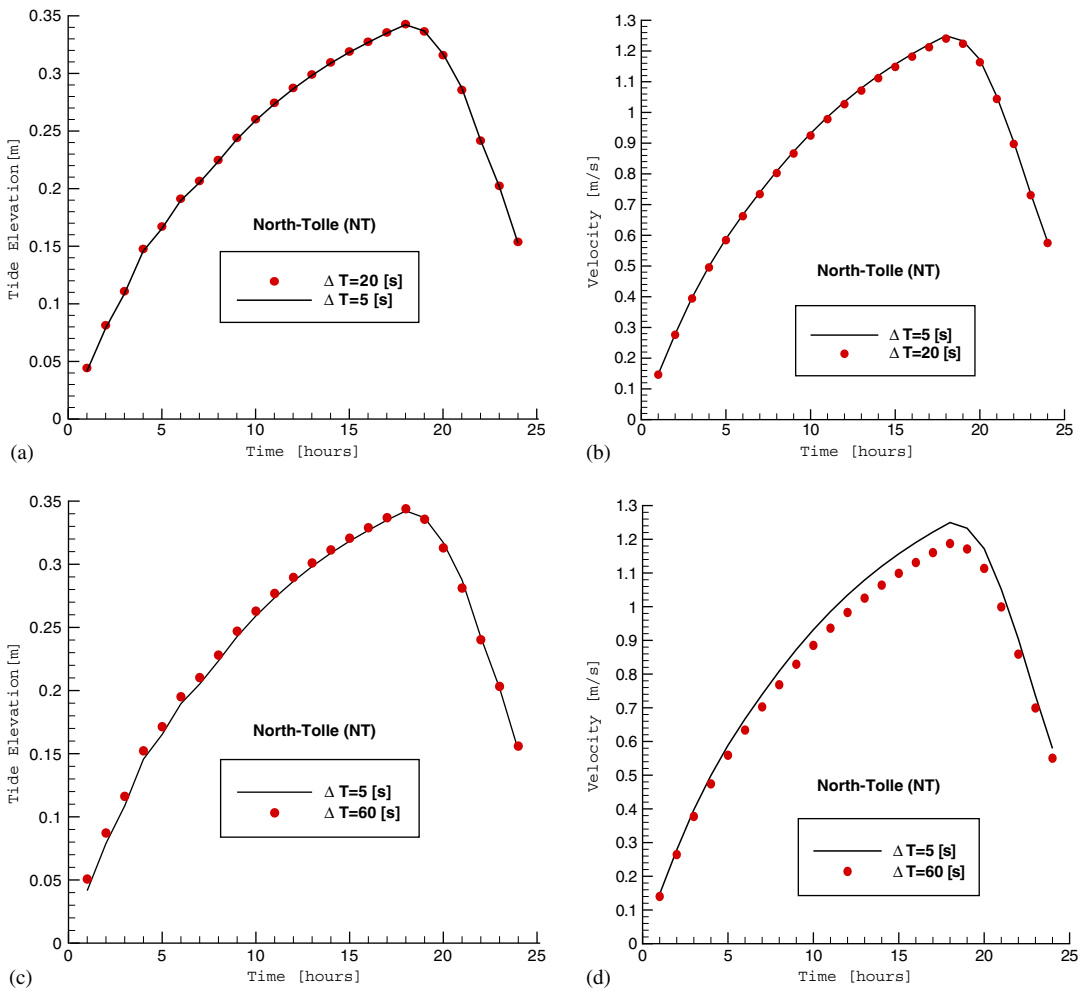

Figure 6. (i) Comparison of tidal level: (a) time steps 5 s *versus* 20 s and (c) time steps 5 s *versus* 60 s; (ii) comparison of velocity: (b) time steps 5 s *versus* 20 s and (d) time steps 5 s *versus* 60 s.

For seabed evolution, a long-period simulation need to be conducted. Generally, the smaller the time step, the higher the accuracy. However, for a small time step, the simulation will require much more computational time.

An efficient splitting scheme is employed to solve hydrodynamic, turbulence, suspended sediment transport, heat and salinity and bed morphology. The present model uses a decoupling between *pure hydrodynamic*, turbulence module, pollutants module and finally the solid phase flow (bed morphology) that are solved in this order (see Figure 2). Thus, the model offers a capability to cope with the stiffness problem introduced by the large difference between the solid phase flow and hydrodynamics time scale.

DOI: 10.1002/fld

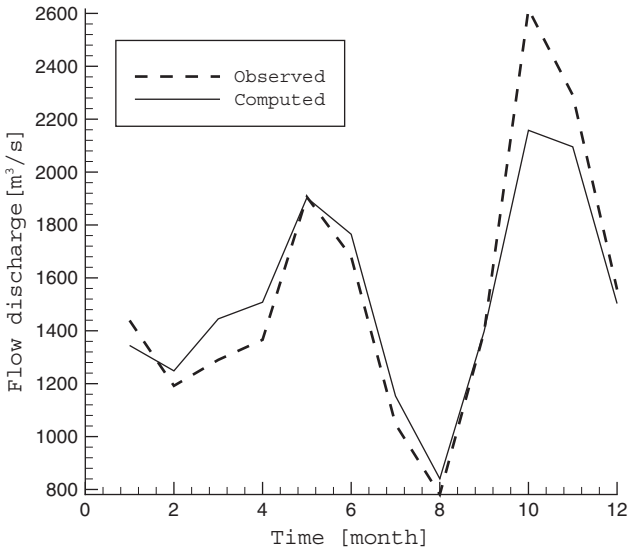

Figure 7. Comparison of the computed and observed current velocities at North-Venezia station (NV) in Po River Estuary (see Figure 4).

For the spatial discretization, we used several lowest layer of thickness δZ_b that should lie within the rough turbulent boundary layer, i.e. $30\nu/u_* < \delta_n = \delta Z_b/2 < 100\nu/u_*$. In the wall region, the shear stress can be assumed constant, $u_* \approx 0.1U$, where U is a flow mean velocity (see [39]) and δ_n is a normal vertical distance of the first vertical mesh point from the bottom.

5.3. Numerical results

Simulations with different time steps have been conducted and the accuracy of numerical results was compared.

Tidal level from the tide gauge and current velocity from tide station North-Tolle (NT) were used to verify the accuracy of the results using three time steps 5, 20, and 60 s. Figure 6 shows the comparison of the tidal level (A), and the current velocity (B) with time steps 5 and 20 s; the comparison of the tidal level (C), and the current velocity (D) with time steps 20 and 60 s. The difference between results is found to be very small. This suggests that the time step of 60 s can produce the accuracy of tidal current similar to the one produced by 5 and 20 s.

It is well known that the k–ε turbulence model needs small time steps, while the bed morphology (solid-phase flow) needs a long-time simulation. The model uses the sub-cycling strategy in the mind of saving computation time. Therefore, several time steps have been set as shown in the flow chart of Figure 2: $\delta t = 60$ s for the *pure hydrodynamic*, one day ($\Delta\tau = 24$ h) for the solid-phase flow (transport of sediment). It is worthwhile to notice that the time step for pollutants, Δt, is a multiple of $\delta t = 60$ s.

Figure 8 shows the comparisons of the computed and observed flow discharge at the tide gauge NT during one year, from January to December 1999. The observed discharge is greater at November corresponding to precipitation maxima. The model predicts well the total water

DOI: 10.1002/fld

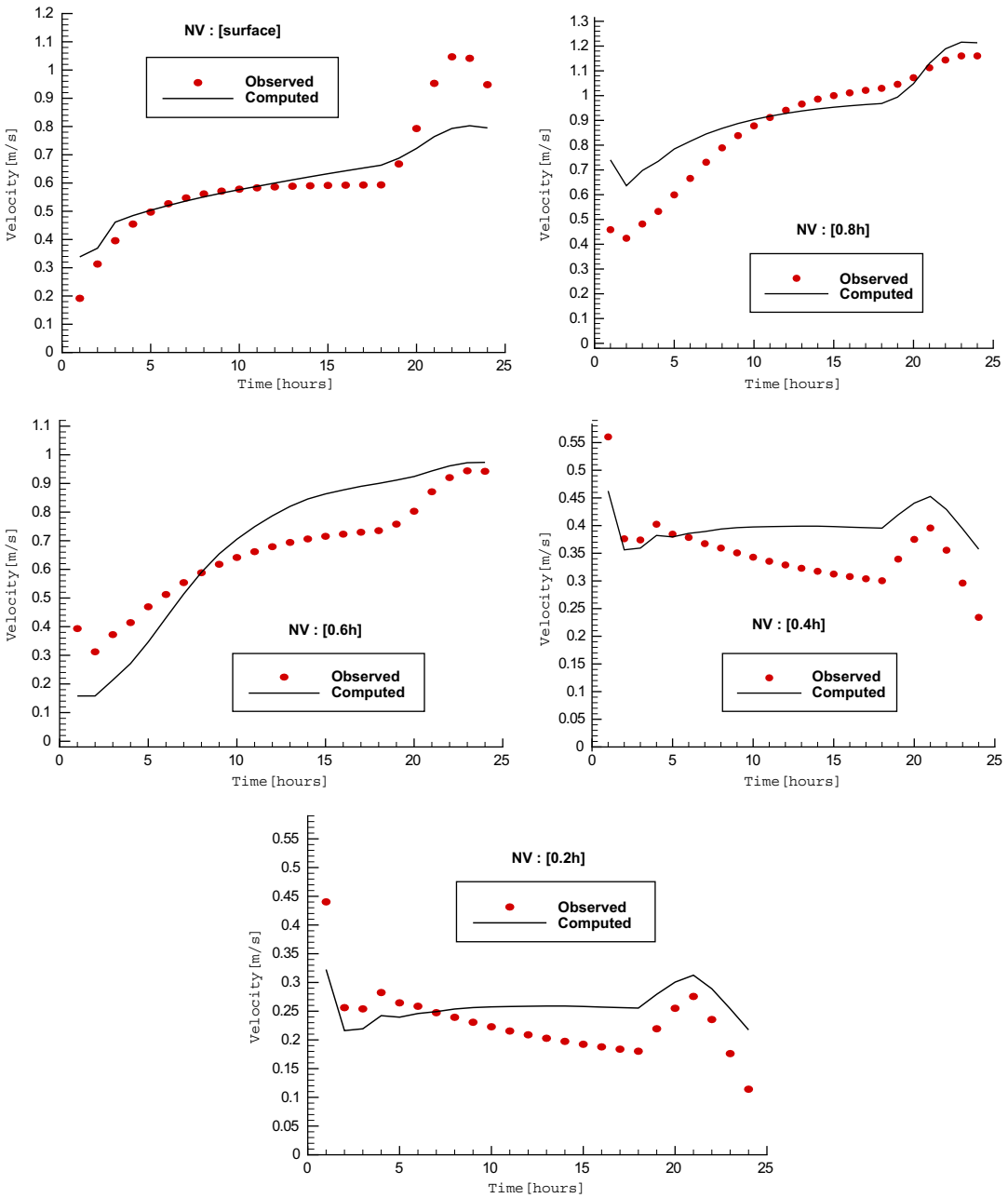

Figure 8. Comparison of the one-year computed and observed flow discharge in Po River Estuary.

DOI: 10.1002/fld

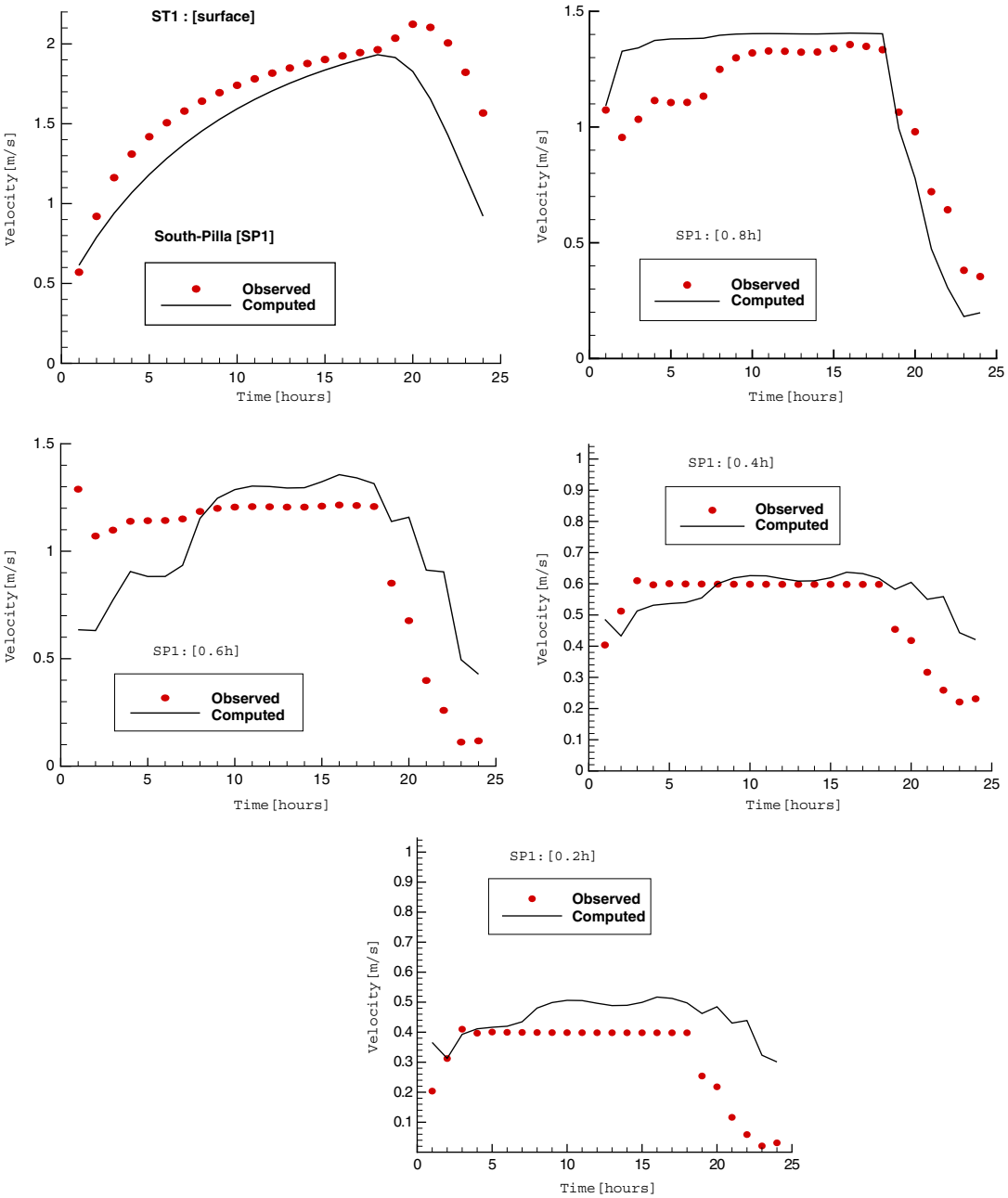

Figure 9. Comparison of the computed and observed current velocities at South-Pilla1 (SP1) station in Po River Estuary.

DOI: 10.1002/fld

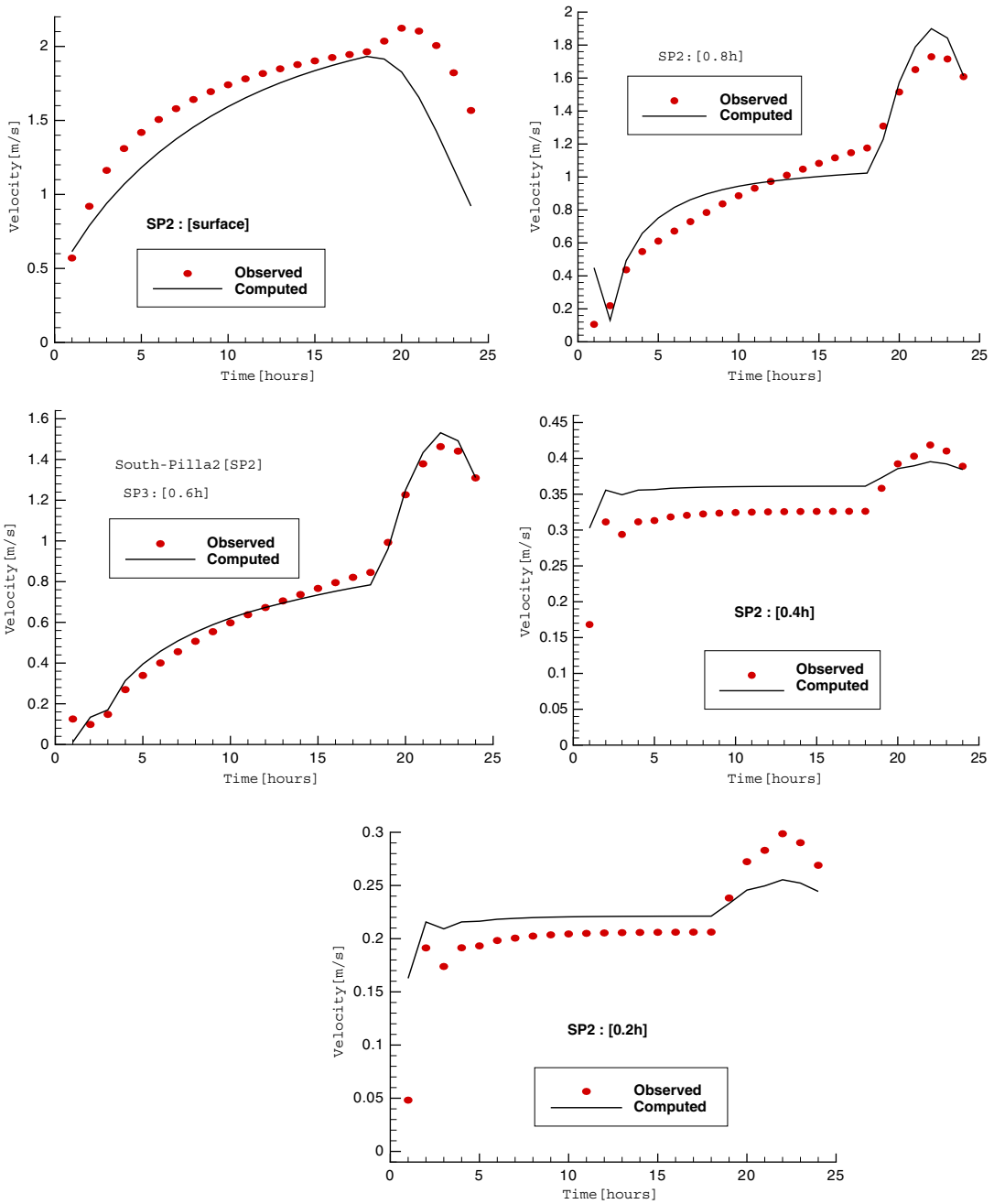

Figure 10. Comparison of the computed and observed current velocities at South-Pilla2 (SP2) station (see Figure 4).

DOI: 10.1002/fld

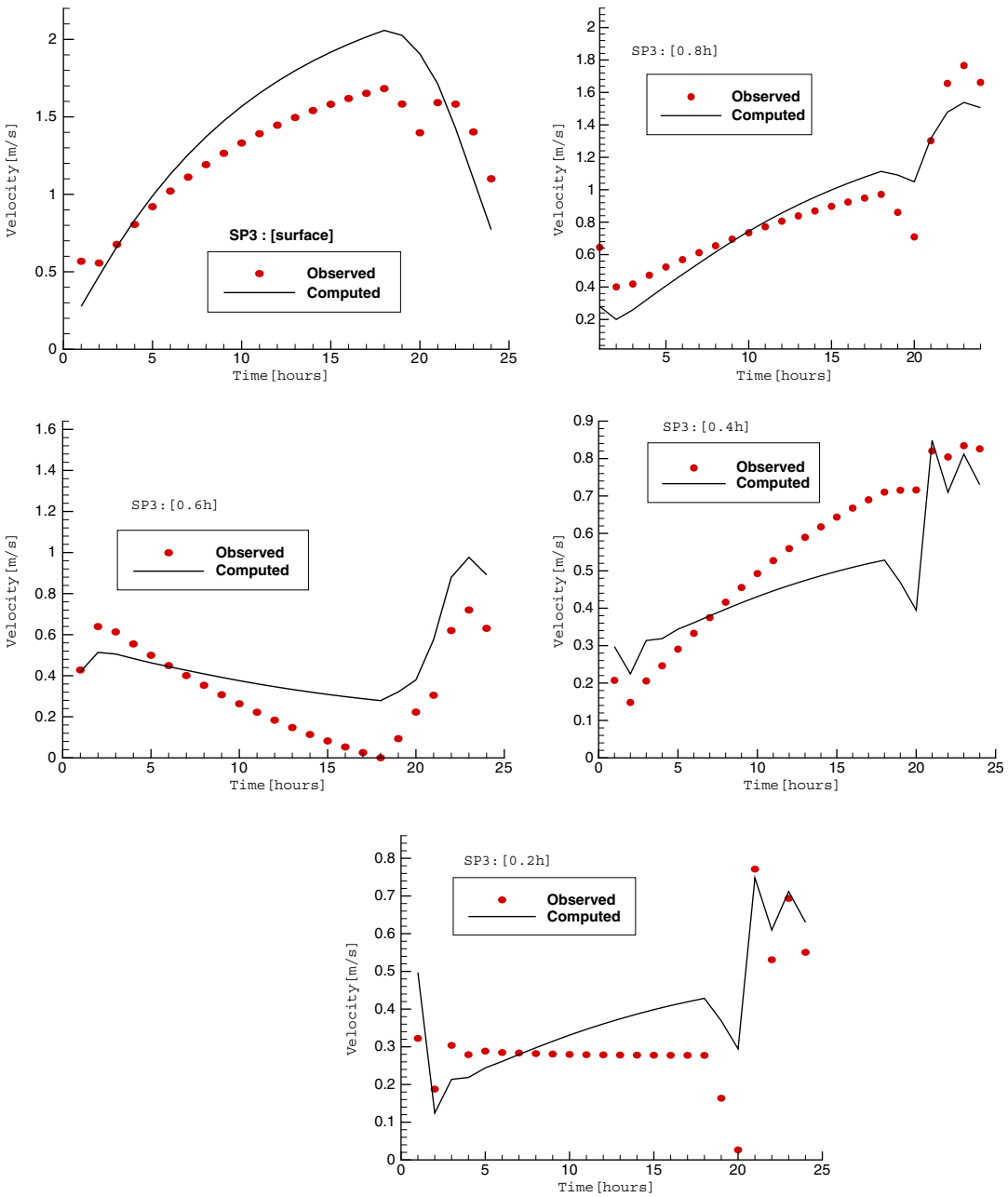

Figure 11. Comparison of the computed and observed current velocities at South-Pilla3 (SP3) station in Po River Estuary (see Figure 4).

DOI: 10.1002/fld

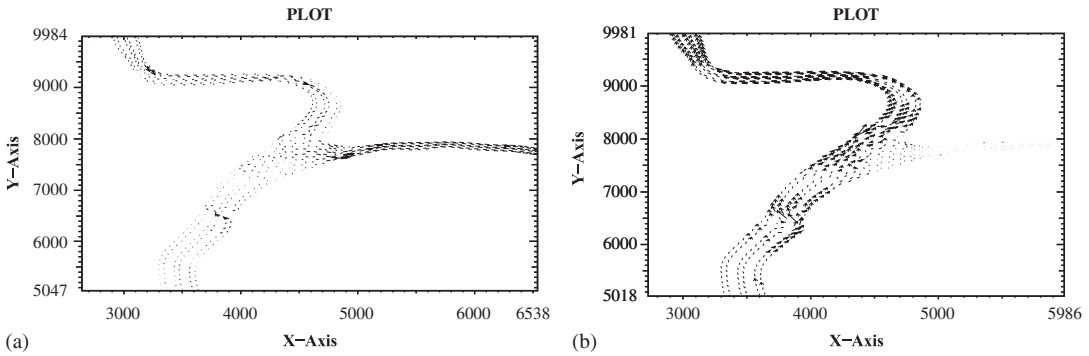

Figure 12. Flow pattern at the bottom in a zone of the domain of study in Po River Estuary at: (a) during flooding and (b) during ebbing.

discharge (the model does not account for meteorological conditions such as precipitation, and this could explain the discrepancy between computations and observations during this period).

Figures 7–11 show the comparisons of the computed and observed flow velocity magnitude at different tide stations and different vertical layers position at, respectively, free-surface, $0.8H$, $0.6H$, $0.4H$ and $0.2H$. Good agreement is found between computed and observed tidal elevations and velocity distributions.

Figure 12 shows a typical ebbing flow pattern and flooding pattern at the bottom in a part of the domain of study. The hydrodynamic computations have shown the ability of the model, thus based on these verifications, a long morphological simulation is performed to predict the seabed evolution, by taking into account the salt, temperature and SSC distribution with the related buoyancy effects on the fluid flow. A wet spring current was chosen for a one-year simulation period. A wet spring current chosen for long periods of one-year simulation is conducted from May 1999 to April 2000, when the river flow is lower during dry season, with the higher precipitation leading to higher pick-up of sediment.

At first, the initial temperature $T_0 = 22.5°\mathrm{C}$ and zero sediment and salt concentration were set in the entire modeled area as, respectively, the initial sediment concentration and salinity (see [42]). An equilibrium distribution is achieved after about one-month simulation, and these values were re-applied as initial sediment, temperature and salinity to predict seabed evolution. Figure 13 shows the predicted profiles of, respectively, the density, temperature and salinity distribution at the selected gauge stations. This figure indicates that the salinity is maximum near the open sea boundary and minimum at the river inlet. The bottom layers are more saline than free-surface layers, as the seawater is encountered in the lower part of the channel, toward the open sea boundaries (see also [48–50]). The upper the layer the smaller the density and salinity, as the higher the temperature (see also [48, 51]). The density profile at the river inlet station North-Venezia (see Figure 4) is quite constant over the water depth. Moreover, the maximum difference between pore water density (ρ) and water density, ρ_0, is found to be about $19\,\mathrm{kg/m^3}$ in the channel. This suggests that PRE is a stable and fairly stratified estuary (see [40, 52]). This mimics the field observations.

The observed suspended sediment discharge is about 16×10^6, and the computed mean suspended sediment discharge using a single function was found to be about 22×10^6 tonnes/year, with mean

DOI: 10.1002/fld

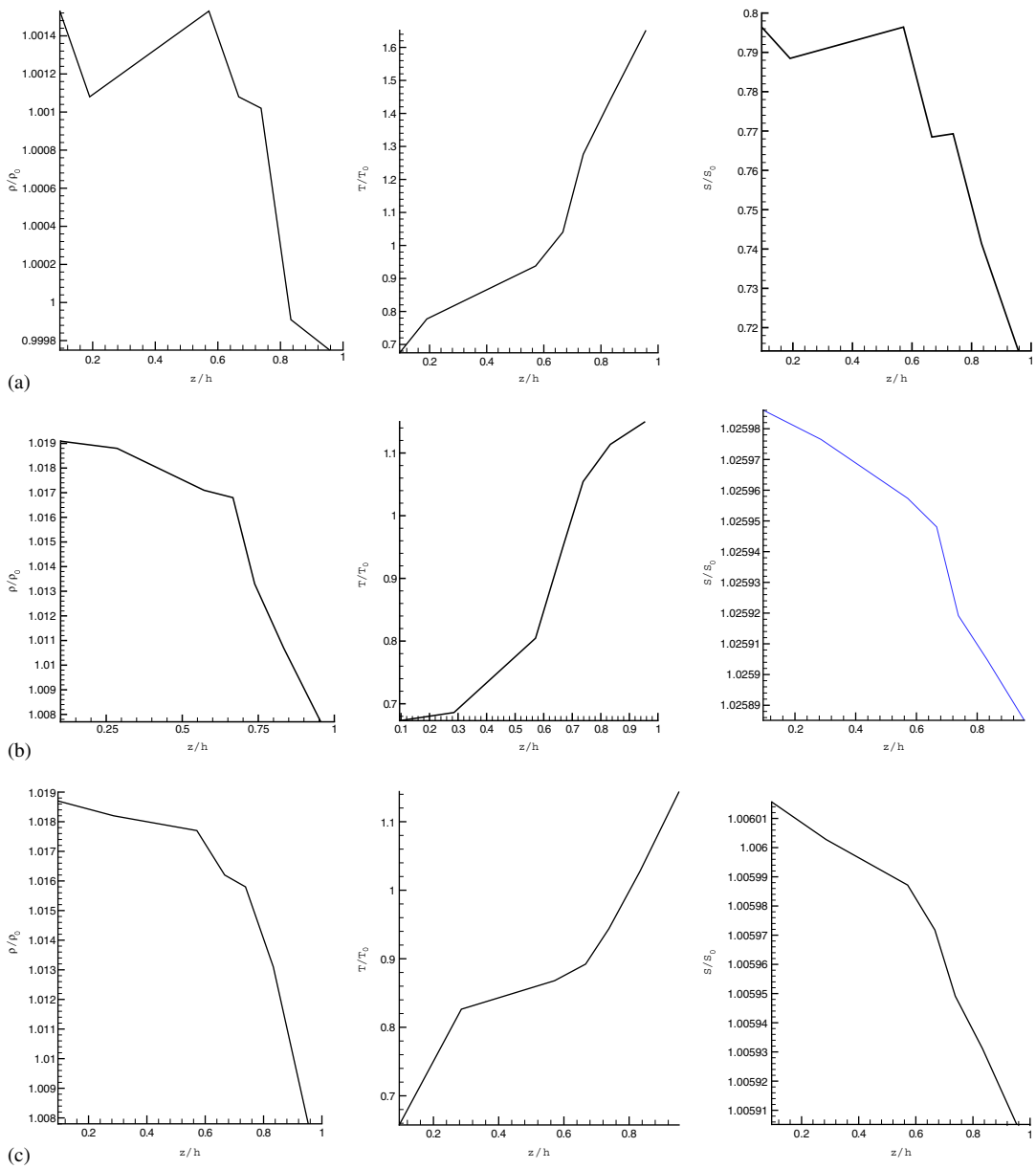

Figure 13. Predicted profiles of fluid density, temperature and salinity after 3 months simulation at the selected gauges stations in Po River Estuary (see Figure 4): (a) North-Venezia (NV); (b) South-Tolle1 (ST1); and (c) South-Pilla1 (SP1).

DOI: 10.1002/fld

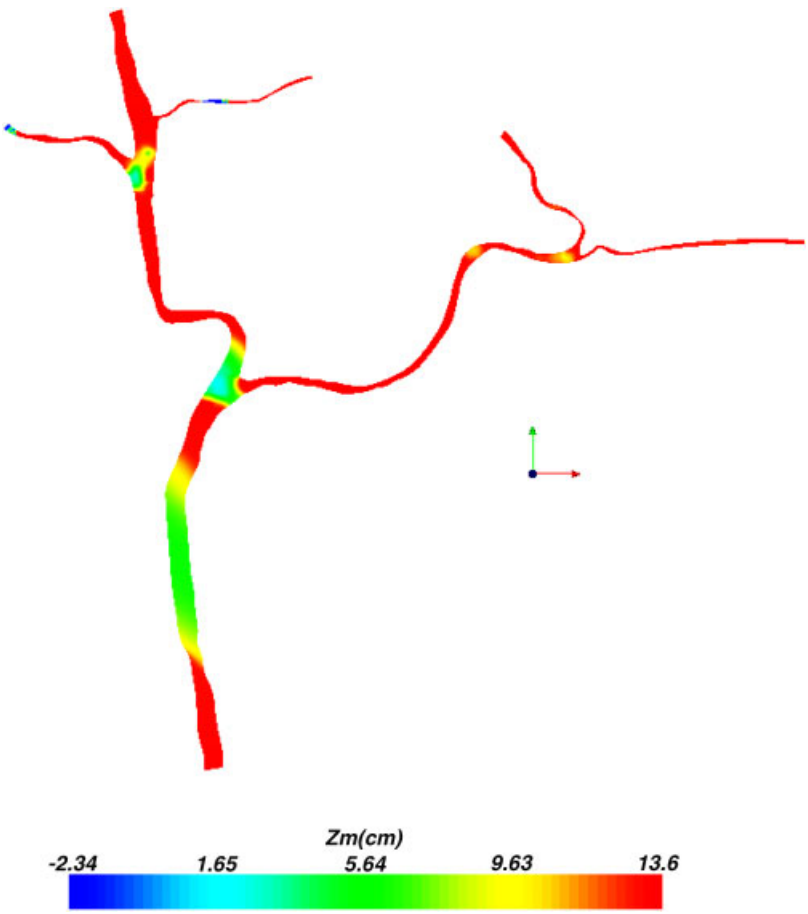

Figure 14. Prediction of the bottom soft-mud layer in Po River Estuary after three months.

SSC of about 250–420 mg/l in the main channel (Panaro-Pilla) and about 80–340 mg/l in the secondary distributaries (South-Pilla and South-Tolle). Figure 14 shows the predicted soft-mud layer at the bottom after three months with the bed thickness ranging between $z_m = -0.023$ and 0.137 m. Computations are found to be in agreement with the field measurements.

6. CONCLUSIONS

A 3D modeling of the cohesive sediment transport and stratified water bodies with environmental forcing is successfully conducted by solving the SWE for incompressible flow using the hydrostatic pressure. The processes modeled include heat, salt and sediment distribution, tidal forcing, surface wind forcing, inflows and outflows as well as the turbulence modeling for multiphasic fluid–solid flow. The present model uses the transport characteristics of the common coarse non-cohesive sediment for predicting cohesive sediments transport in PRE. The micro-tidal PRE (i.e. tidal

DOI: 10.1002/fld

elevation <2 m) is found to be a fairly stratified estuary, with the estuarine turbidity maximum (ETM), i.e. near-bed concentrations of 80–420 mg/l.

The water elevation and velocity field computed from the numerical models were compared successfully to observed data, while temperature, salinity and sediment concentration profiles are found to be realistic.

The model predicts realistically the complex major features and their consequences on the flows in PRE in Italy. However, further application, using more suitable characteristics transport functions for cohesive sediments, is needed to improve the general applicability of the model, and this will be the next stage of this work.

ACKNOWLEDGEMENTS

The first author acknowledged funding from the Swiss National Science Foundation through grant number 21-65095.01. Edie Miglio and Alfio Quarteroni are acknowledged for their fruitful discussions.

REFERENCES

1. Lie-Yauw O, Mellor LG. A three-dimensional simulation of the Hudson–Raritan estuary. Part II: description of the model and model simulations. *Journal of Physical Oceanography* 1985; **15**:1676–1692.
2. Lie-Yauw O, Mellor LG. A three-dimensional simulation of the Hudson–Raritan estuary. Part I: comparison with observation. *Journal of Physical Oceanography* 1985; **15**:1693–1709.
3. Lu QM, Wai WHO. An efficient operator splitting scheme for three-dimensional hydrodynamics computations. *International Journal for Numerical Methods in Fluids* 1998; **26**:771–789.
4. Chau KW, Jiang YW. 3D Numerical model for Pearl River estuary. *Journal of Hydraulic Engineering* 2001; **127**(1):72–82.
5. Chau KW, Jiang YW. A three-dimensional pollutant transport model in orthogonal curvilinear and sigma coordinate system for Pearl River estuary. *International Journal of Environmental Pollution* 2004; **21**(2):188–199.
6. van Rijn LC. Mathematical modeling of suspended sediment in non uniform flows. *Journal of Hydraulic Engineering* 1986; **112**:433–455.
7. van Rijn LC. Field verification of 2D and 3D suspended-sediment models. *Journal of Hydraulic Engineering* 1986; **116**:1270–1288.
8. Roberts W. Development of mathematical model of fluid mud in the coastal zone. *Proceedings of the Institution of Civil Engineers*, *Water Maritime and Energy*, Wallingford, 1993; 173–181.
9. Ziegler CK, Nisbet B. Fine-grained sediment transport in Pawtuxet, Rhode Island. *Journal of Hydraulic Engineering* 1994; **120**:561–576.
10. Guan WB, Wolanski E, Dong LX. Cohesive sediment transport in Jiaojiang River estuary, China. *Estuarine*, *Coastal and Shelf Science* 1998; **46**:861–871.
11. Lin BI, Falconner RA. Numerical modeling of three-dimensional suspended sediment for estuarine and coastal waters. *Journal of Hydraulic Research* 1996; **34**:435–456.
12. Chen Y, Wai OWH, Li YS, Lu Q. Three-dimensional numerical modeling of cohesive sediment transport by tidal current in Pearl River estuary. *International Journal of Sediment Research* 1999; **14**:107–123.
13. Luyten PJ, Jones JE, Proctor R, Tabor A, Tett P, Wild-Allen K. COHERENS—A coupled hydrodynamical–ecological model for regional and shelf seas: user documentation. *MUMM Report*, Management Unit of the Mathematical Models of North Sea, 1999; 914.
14. Teisson C, Simonin O, Galland JC, Laurence D. Turbulence and mud sedimentation: a Reynolds stress model and a two-phase flow model. *Proceedings of the 23rd International Conference on Coastal Engineering* 1992; 2853–2866.
15. Le Hir P. Fluid and sediment integrated-modelling. Application to fluid mud flows in estuaries. *Proceedings of Nearshore and Estuarine Cohesive Sediment Transport Conference*, *INTERCOH 94*, Wallingford. Paper 41. Wiley: Chichester, 1994.
16. Uittenbogaard RE, Winterwerp JC. 3D cohesive sediment transport. *Report Z1022*, Delft Hydraulics Laboratory, 1996.

DOI: 10.1002/fld

17. Olsen RB, Skoglund M. Three-dimensional numerical modeling of water and sediment flow in a sand trap. *Journal of Hydraulic Research* 1994; **36**:833–844.
18. Huang JW. The experimental study of the scouring and settling properties of cohesive sediment. *Ocean Engineering* 1989; **7**:61–70.
19. Dyer KR. Sediment processes in estuaries: future research requirements. *Journal of Geophysical Research* 1989; **94**:14327–14339.
20. Van Leussen W, Corneliss JM. The determination of the sizes and settling velocities of estuarine flocs by an underwater video system. *Netherlands Journal of Sea Research* 1993; **31**:231–241.
21. Malcherek A, Markofsky M, Zielke W. Numerical modelling of the particle size distribution in estuaries. *Proceedings of the International Symposium Part*, Reinbek, 1994.
22. Tang CB. The law of sediment initiation. *Shuili Xuebao* 1963; **2**:113–133 (in Chinese).
23. Mehta AJ, Srinivas R. Observations on the entrainment of fluid mud by shear flow. *Nearshore and Estuarine Cohesive Sediment Transport*. AGU: Washington, 1992; 224–246.
24. Casulli V. Semi-implicit finite difference methods for the two-dimensional shallow equations. *Journal of Computational Physics* 1990; **86**:56–74.
25. Casulli V, Cheng RT. Semi-implicit finite difference methods for three-dimensional shallow water flow. *International Journal for Numerical Methods in Fluids* 1992; **15**:629–648.
26. Leupi C, Altinakar SM. Finite element modeling of free-surface flows with non hydrostatic pressure and k–epsilon turbulence model. *International Journal for Numerical Methods in Fluids* 2005; **49**:149–170.
27. Roland S. *Modélisation et Simulation des Ecoulements Turbulents*. Hermes: Paris, 1993.
28. Rodi W. *Turbulence Models and their Application in Hydraulics* (2nd edn). International Association for Hydraulic Research: Delft, The Netherlands, 1984.
29. Leupi C. Numerical modeling of cohesive sediment transport and bed morphology in estuaries. *Ph.D. Thesis no. 3266*, EPFL, Lausanne, Switzerland, 2005.
30. Mohammadi B, Pironneau O. *Analysis of k–epsilon Turbulence Model*. Wiley: Chichester, 1994.
31. Luyten PJ, Deleesnijder E, Ozer J, Ruddick KG. Presentation of a family of turbulence closure models for stratified shallow water flows and preliminary application to the Rhine outflow region. *Continental Shelf Research* 1996; **16**:101–130.
32. Leupi C, Miglio E, Altinakar M, Quarteroni A, Deville M. QUASI-3D finite element shallow-water flow with k–ε turbulence model. *Proceedings of the International Conference on Advances in Hydro-science and -Engineering, ICHE*-vol. 6, Brisbane, Australia, 2004, 2003; 400–401 (CD-ROM).
33. Stansby PK, Zhou JG. Shallow-water flow solver with nom-hydrostatic pressure: 2D vertical plane problems. *International Journal for Numerical Methods in Fluids* 1998; **28**:541–563.
34. Coleman NL. Flume studies of the sediment transfer coefficient. *Water Resources Research* 1970; **6**(3):301–809.
35. van Rijn LC. Mathematical Modelling of Morphological Processes in the case of Suspended Sediment Transport, vol. 382. Delft Hydraulics Laboratory, 1987; 1613–1639.
36. van Rijn LC. Transport of fine sands by currents and waves. *Journal of Waterway*, *Port*, *Coastal and Ocean Engineering* 1993; **121**:113–133.
37. Migniot C. A study of the physical properties of various forms of very fine sediment and their behaviour under hydrodynamics action. *La Houille Blanche* 1968; **7**:591–620.
38. Dou GR. A suspended sediment numerical modelling under wave and tidal current. *Workshop on Ocean Engineering* 1995; 97–111.
39. Graf WH, Altinakar MS. *Hydraulique Fluviale*. Presses Polytechniques et Universitaires Romandes: Lausanne, Switzerland, 1993.
40. Graf WH, Altinakar MS. *Hydraulique Fluviale*. Presses Polytechniques et Universitaires Romandes: Lausanne, Switzerland, 1996.
41. Raviart PA, Thomas JM. A mixed finite element method for 2nd order elliptic problems. In *Mathematical Aspects of Finite Element Methods*, Galligani I, Magenes E (eds). Lecture Notes in Mathematics. Springer: Berlin, 1977; 292–315.
42. Kettner AJ, Syvistki JPM. Predicting discharge and sediment flux of the Po river, Italy since the Late Glacial maximum. *Technical Report*, *CO 80309-0450*, University of Colorado, 2004.
43. Gabianelli G. Marina di Ravenna Lido Adriano (Italy): IAHS publication No. 151. CENAS Project (2nd edn). Interdepart. Centre for Environmental Science, Bologna University, IAHR, Delft, Netherlands, 1997; 1–17.
44. Marchi E, Roth G, Siccardi F. The Po: centuries of river training. *Physics and Chemistry of the Earth* 1996; **20**:475–478.

DOI: 10.1002/fld

45. Cattaneo A, Correggiari A, Langone L, Trincardi F. The late-Holocene Gargano subaqueous delta, Adratic shelf: sediment pathways and supply fluctuations. *Marine Geology* 2003; **193**:61–91.
46. ENDEAVOUR. Salt intrusion control: Po Di Gnocca River Project-Italy. *Technical Report*, ENDEAVOUR-44030 Fossaltat Ferrara/Italia, 1986; 1–17.
47. Viganó L. The sediment quality of the Po River and the Italian Decree No. 152/99 for the protection of aquatic environments. *Ann Ist Super Sanitá* 2002; **32**:137–141.
48. Holt JT, James ID. A simulation of the Southern North Sea in comparison with measurements from the North Sea project. Part I: temperature. *Continentals Shelf Research* 1999; **19**:1087–1112.
49. Hills PS. Reconciling aggregation theory with observed vertical fluxes following phytoplankton blooms. *Journal of Geophysical Research* 1992; **97**:2295–2308.
50. Chau KW. A three-dimensional eutrophication modeling in Tolo Harbor. *Applied Mathematical Modelling* 2004; **28**(9):849–861.
51. Lung W, Martin JL, McCutheon SC. Eutrophication analysis of embayment in Prince William sound, Alaska. *Journal of Environmental Engineering* (ASCE) 1993; **119**(5):811–824.
52. Steinhorn I. Salt flux and evaporation. *Journal of Physical Oceanography* 1991; **21**:1681–1683.

DOI: 10.1002/fld